REVIEW SUMMARY

OPTICS

Ultraslow waves on the nanoscale

Kosmas L. Tsakmakidis,* Ortwin Hess, Robert W. Boyd, Xiang Zhang*

BACKGROUND: The past 10 to 15 years have witnessed substantial advances in our ability to controllably adjust, slow down, or accelerate the speed of light signals propagating through dispersive optical media. In the fields of optoelectronics and photonics, we have for decades been accustomed to using propagating or guided light waves with speeds only slightly less than the speed of light in a vacuum, c—usually by a factor of 2 to 4. We now know that the group velocity of light waves entering a highly dispersive medium can be reduced by a factor of millions, down to the "human" scale, by exploiting judicious interference effects at the atomic scale of the material. Light decelerations by a factor of a few hundred, with low losses, can be attained in periodic dielectric structures, such as photonic crystal and coupled-resonator optical waveguides. Enabled applications include all-optical tunable delays for routers and data synchronization, optical buffers, enhanced light-matter interaction and nonlinear effects, and miniaturized photonic devices, such as modulators and interferometers. However, such atomic- or dielectric-media–based "slow light" is still fundamentally limited by the wavelength of light, λ, to spatial dimensions larger than ~$\lambda/2$ (~300 nm for visible light)—i.e., it is still diffraction limited and cannot reach true nanoscopic dimensions (e.g., below ~30 nm). It is at this point that media featuring negative electromagnetic parameters, such as negative-permittivity plasmonic media or negative–refractive index metamaterials, come to the rescue.

ADVANCES: Light deceleration in these media arises from the presence of a negative (real part of) electric permittivity, ε, or refractive index, n, leading to antiparallel power flows in the negative-parameter medium and the surrounding dielectric host—thereby giving rise to energy and group velocities that can be reduced even down to zero for a suitable choice of optogeometric parameters. This mechanism for slowing down light is thus nonresonant, and as such it can be broadband, with typical bandwidths being on the order of ~1 to 10 THz. Most notably, these structures support ultraslow surface-plasmon or surface-phonon polaritons that can be concentrated tightly into the nanoscale, at nanovolumes (at least) thousands of times smaller than λ^3, upon suitable adiabatic tapering. This leads to large local field enhancements, of the order of 10^2 to 10^3, over small nanovolumes that can be exploited for a host of useful applications, including nanoimaging, biosensing and nanoscale chemical mapping, high-density magnetic data-storage recording, light harvesting, nanolasing, and nanoscale quantum and nonlinear optics. One must be mindful, though, of targeting applications (such as the ones mentioned above) for which dissipative losses, which are normally higher in these media compared to their dielectric counterparts, are not a prohibitive factor—i.e., applications for which energy efficiency is not the key figure-of-merit.

ON OUR WEBSITE

Read the full article at http://dx.doi.org/10.1126/science.aan5196

OUTLOOK: Thus far, this method of nanoscale, broadband slow light has relied on the use of uniform or nanostructured metals (plasmonic media), but continued advances in materials design and synthesis have recently enabled a transition to alternative media, such as doped semiconductors, graphene, hexagonal boron nitride, transition-metal dichalcogenides (such as TaS_2), van der Waals crystals, and heterostructures. There are important ongoing efforts to push the response of these alternative media, which is currently mainly in the mid- and near-infrared regimes, into the visible region as they allow for considerably lower losses and enhanced controllability (e.g., simply by application of a gate voltage). With these new material platforms, opportunities for new applications emerge, too, particularly those requiring nanoscale (and even atomic) confinements and ultrahigh field enhancements, such as low-threshold single-photon nonlinearities and applications relying on the generation and manipulation of nonclassical light, at ambient conditions. ■

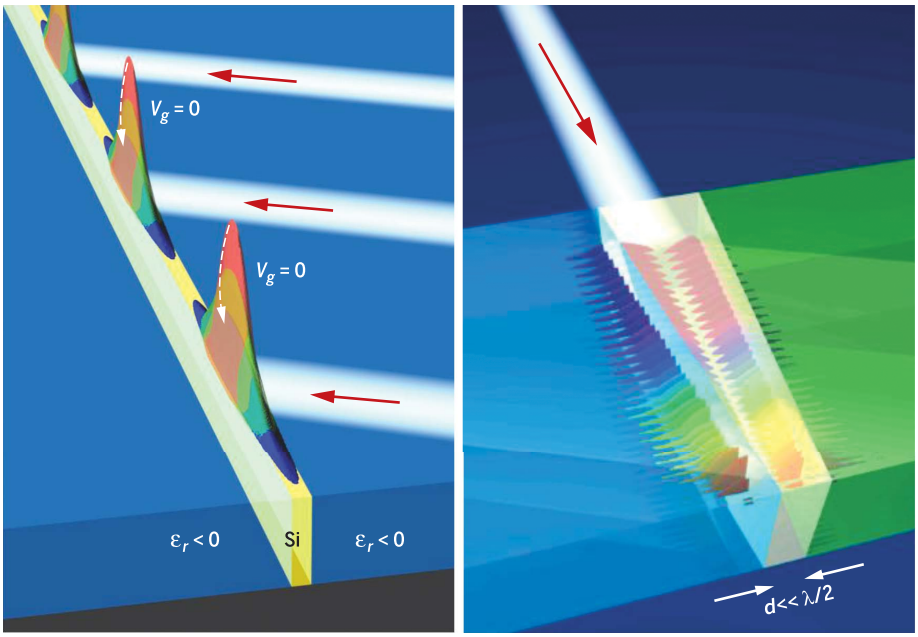

Broadband subdiffraction ultraslow and stopped light. (Left) Light beams incident (red arrows) on a Si film bounded symmetrically by a negative-permittivity (plasmonic) medium ($\varepsilon_r < 0$) excite guided light pulses that can have zero group velocity, v_g, decaying with time (dashed arrows) exactly at their injection points rather than propagating along the Si film. (Right) Surface plasmon polaritons propagating along an adiabatically tapered plasmonic nanoguide (white prism) are slowed down over a broad range of frequencies ("colors"), accumulating at a deep-subdiffraction spot ($d << \lambda/2$) at the tip of the guide and leading to large local field enhancements.

The list of author affiliations is available in the full article online.
*Corresponding author. Email: kostsakmakidis@gmail.com (K.L.T.); xiang@berkeley.edu (X.Z.)
Cite this article as K. L. Tsakmakidis *et al.*, *Science* **358**, eaan5196 (2017). DOI: 10.1126/science.aan5196

REVIEW

OPTICS

Ultraslow waves on the nanoscale

Kosmas L. Tsakmakidis,[1*†] Ortwin Hess,[2] Robert W. Boyd,[3] Xiang Zhang[1,4,5*]

There has recently been a surge of interest in the physics and applications of broadband ultraslow waves in nanoscale structures operating below the diffraction limit. They range from light waves or surface plasmons in nanoplasmonic devices to sound waves in acoustic-metamaterial waveguides, as well as fermions and phonon polaritons in graphene and van der Waals crystals and heterostructures. We review the underlying physics of these structures, which upend traditional wave-slowing approaches based on resonances or on periodic configurations above the diffraction limit. Light can now be tightly focused on the nanoscale at intensities up to ~1000 times larger than the output of incumbent near-field scanning optical microscopes, while exhibiting greatly boosted density of states and strong wave-matter interactions. We elucidate the general methodology by which broadband and, simultaneously, large wave decelerations, well below the diffraction limit, can be obtained in the above interdisciplinary fields. We also highlight a range of applications for renewable energy, biosensing, quantum optics, high-density magnetic data storage, and nanoscale chemical mapping.

More than 100 years ago, in 1914, Sommerfeld, Brillouin, and Lorentz started investigating situations in which the group velocity v_g of light signals exceeds the vacuum speed of light, c, leading to what they initially thought were apparent inconsistencies with Einstein's special theory of relativity (*1*–*3*). The group velocity of a wave packet propagating inside a dispersive medium of refractive index n is given by $v_g = c/n_g$, where $n_g = n + \omega(dn/d\omega)$ is the group refractive index of the medium, with ω being the angular frequency, from which it is seen that in the region of anomalous dispersion in a normal absorbing medium, where $dn/d\omega < 0$, v_g may exceed c—but with high losses (*4*–*7*). More recently, experimental observations of superluminal group velocities have been reported in the propagation of mode-locked pulse trains in resonant absorbers (*8*) and in photon tunneling from potential barriers (*9*, *10*). Furthermore, distortionless superluminal pulse propagation with minimal amplitude change has been observed in gain doublets (*11*), together with evanescent-wave superluminal group velocities at the cutoff of microwave waveguides (*12*), and superluminal effects arising solely from the nature of the propagating field, such as in the propagation of Bessel beams (*5*, *13*). None of these situations violates relativistic causality as in all cases the front velocity—the velocity with which a discontinuity in a waveform or one of its derivatives propagates—is smaller than c (*5*, *9*).

The opposite phenomenon, in which the group velocity of a light wave can become much smaller than c, was also identified and studied (*3*–*6*, *14*). For instance, within a hollow waveguide, the wave vector β along the guide is reduced below the free-space value, leading to a phase velocity $v_\varphi = \omega/\beta$ greater than c. But within such a structure, the product of the phase and the group velocities is given as (*15*) $v_\varphi v_g = c^2$, thereby resulting in a group velocity along the guide that can become considerably smaller than c. A further intuitive example is epsilon-near-zero media (*16*), in which the electric permittivity $\varepsilon(\omega_0) \to 0$ at a frequency ω_0. In such media, the wave vector $k = (\omega/c)\sqrt{\varepsilon(\omega)}$ becomes zero at ω_0, hence the phase velocity v_φ becomes infinite, but the group velocity $v_g = (dk/d\omega)^{-1} = c\left[\sqrt{\varepsilon(\omega)} + \omega/\left(2\sqrt{\varepsilon(\omega)}\right)\right]^{-1}$ becomes zero at $\omega = \omega_0$ (*17*, *18*)—a property that can be exploited for boosting light-matter interactions and nonlinear effects (*16*).

Much of the impetus for the contemporary interest in such "slow" and "fast" light phenomena was provided by the 1999 experiment by Hau *et al.* (*19*), which demonstrated that the speed of light in atomic electromagnetically induced transparent (EIT) media could be reduced to the "human" scale of ~17 m/s—albeit over very narrow bandwidths (*20*), typically of the order of a few tens of kilohertz. Thereafter, a range of solid-state systems were proposed and investigated for slowing down the speed of guided light signals, including photonic crystal (PhC) waveguides (*21*, *22*), coupled resonator optical waveguides (CROWs) (*23*), and standard optical fibers (*24*, *25*). These slow-light structures exhibit fascinating fundamental physics and have enabled a range of useful applications underpinned by the strong (and broadband) light-matter interactions that they entail (*26*–*28*). However, they are fundamentally limited by the wavelength of light—i.e., they are diffraction limited, and cannot reach true nanoscopic dimensions, e.g., scales less than ~30 nm.

More recently, media exhibiting negative electromagnetic or optical parameters (such as negative permittivity and/or refractive index) (*29*–*31*) have emerged as a new means of allowing large and broadband light decelerations—but, this time, well below the diffraction limit, right at the nanoscale, where a host of new material properties, functionalities, applications, and opportunities emerge. These media typically feature higher losses compared with their dielectric counterparts; thus, one has to be mindful of targeting applications that can be more loss tolerant (*32*, *33*). We will focus on wave-deceleration methods that allow—on the basis of the same underlying mechanisms in all cases—for simultaneously broadband operation and small group velocities, below the diffraction limit, so that the nanoscale can be reached, in nanophotonic media, metamaterials, graphene, van der Waals crystals, and heterostructures. We detail the broadband mechanisms, not involving bulk-material parameter (permittivity, refractive index) resonances, by which subdiffraction waves of various kinds can be slowed down in the aforementioned structures, their unique characteristics, and how these are exploited in a host of applications across the fields of optics and photonics, acoustics, and two-dimensional (2D) condensed matter.

Physics of subdiffraction slow and stopped light waves

Almost all types of nanoscale guiding structures inherently feature slow waves of some kind—light/photons, guided Dirac fermions, surface plasmon polaritons (SPPs), or surface phonon polaritons. This section reviews the physical mechanisms by which extremely slow light or SPPs can be obtained over broad spectral ranges through use of suitably engineered and nanophotonic media that confine the light field to dimensions smaller than the conventional diffraction limit (*34*–*36*).

Unlike atomic schemes (*19*, *37*, *38*) or periodic dielectric structures (*21*–*23*, *26*–*28*), which are usually diffraction limited (*34*, *35*), this route does not entail bulk-material resonances, disorder, or periodic back reflections to slow or stop light. The deceleration can occur even in longitudinally uniform (nonperiodic) structures, and away from intrinsic material resonances—e.g., in a regime where the real part of the permittivity, ε, of a heterostructure's layer is negative, following a nonresonant Drude variation (*39*). Such structures can be either metamaterial or plasmonic waveguides (*36*, *39*–*62*) (Fig. 1, A to C). For transverse magnetic (TM) polarization, the time-averaged complex Poynting vector in the longitudinal z direction of a metamaterial waveguide (Fig. 1A), $\bar{S}_z$, is given by $\bar{S}_z = \frac{1}{2}\mathrm{Re}\{\mathbf{E} \times \mathbf{H}^*\}_z = \frac{\beta}{2\omega\varepsilon_0\varepsilon_i}|H_y|^2$,

[1]NSF Nanoscale Science and Engineering Center (NSEC), University of California at Berkeley, 3112 Etcheverry Hall, Berkeley, CA, USA. [2]The Blackett Laboratory, Department of Physics, Imperial College London, London SW7 2AZ, UK. [3]Department of Physics and School of Engineering and Computer Science, University of Ottawa, Ottawa, Ontario K1N 6N5, Canada. [4]Material Sciences Division, Lawrence Berkeley National Laboratory, 1 Cyclotron Road, Berkeley, CA 94720, USA. [5]Department of Physics, King Abdulaziz University, Jeddah 21589, Saudi Arabia.
***Corresponding author. Email: kostsakmakidis@gmail.com (K.L.T.); xiang@berkeley.edu (X.Z.)** †Present address: Bioengineering Department, EPFL, 1015 Lausanne, Switzerland, and Department of Solid State Physics, National and Kapodistrian University of Athens, Panepistimioupolis, GR - 157 84, Athens, Greece.

where β is the longitudinal propagation constant, ε_i is the layers' dielectric permittivities, and i is the core layer or cladding layer (*43*). Thus, in the negative-permittivity (and negative–refractive index) core layer of this symmetric, lossless waveguide, $\bar{S}_{z,co} < 0$, whereas in the positive-permittivity dielectric cladding layers, $\bar{S}_{z,cl} > 0$. Hence, the total time-averaged power flow, $P = \int_{-\infty}^{\infty} \bar{S}_z dx$, in the $+z$ direction will be reduced owing to the negative contribution from $\bar{S}_{z,co}$, and can even become zero when $|\bar{S}_{z,co}| = 2\bar{S}_{z,cl}$. But in a lossless dispersive medium (or waveguide), the energy velocity, v_E, is equal to the group velocity, v_g, and is given by $v_E = P/U$, with U being the energy density (*5*, *6*, *63*). Therefore, as a result of the antiparallel power flows in the core and cladding layers of this waveguide, both its energy and group velocities can be reduced to zero. As shown in Fig. 1A, the structure of the instantaneous Poynting vector **S** on the xz plane of the guide takes on a vortex form at each interface, with energy flowing back and forth across each interface but, on average, with no net energy being transported across each interface. Indeed, a straightforward calculation shows that the curl of **S**, which characterizes its vorticity, is nonzero and is given by $\nabla \times \mathbf{S} = (\rho_s/\varepsilon_0)H_y\hat{\mathbf{y}}_0$, where ρ_s is the surface polarization charge density. Thus, the curl of the Poynting vector field is zero in both the negative–refractive index core and dielectric cladding layers, and is nonzero (and maximum) only at the two interfaces, as inferred directly from Fig. 1A.

Figure 1B illustrates a further example of light slowing down at the nanoscale, this time in an adiabatically tapered plasmonic nanoguide (*41*, *42*). SPPs guided along this nanocone are progressively decelerated until their group velocity becomes zero at the structure's tip, where they accumulate (*41*). The SPPs are longitudinally and laterally compressed as they reach the tip, with the electric field being largely enhanced in that region, deep below the diffraction limit. Both of these nanoscale slow-light mechanisms—the double-vortex structure in the power flux vector and the use of a tapered structure to accumulate light in a subdiffraction spot—underpin many of the underlying physics and applications that this type of light-deceleration features.

Slow light in these media is typically broadband, with Fig. 1C illustrating a tapered negative-index metamaterial waveguide capable of halting a "rainbow" of light wavelengths at predefined critical points (*43*). Here, a light ray is forced by the negative electromagnetic "environment" that it experiences in the core layer of the guide to make, in each half period, a forward "step" followed by a negative phase-shift step. At the zero–group-velocity point, the negative Goos-Hänchen phase shifts bring the light ray precisely back to its initial position. The Goos-Hänchen phase shift arises when a finite-width beam (i.e., not a laterally infinitely extended plane wave) is totally internally reflected at the interface of two media (e.g., from a high-, negative-permittivity ε medium "1" to a lower-, positive-permittivity medium "2,"

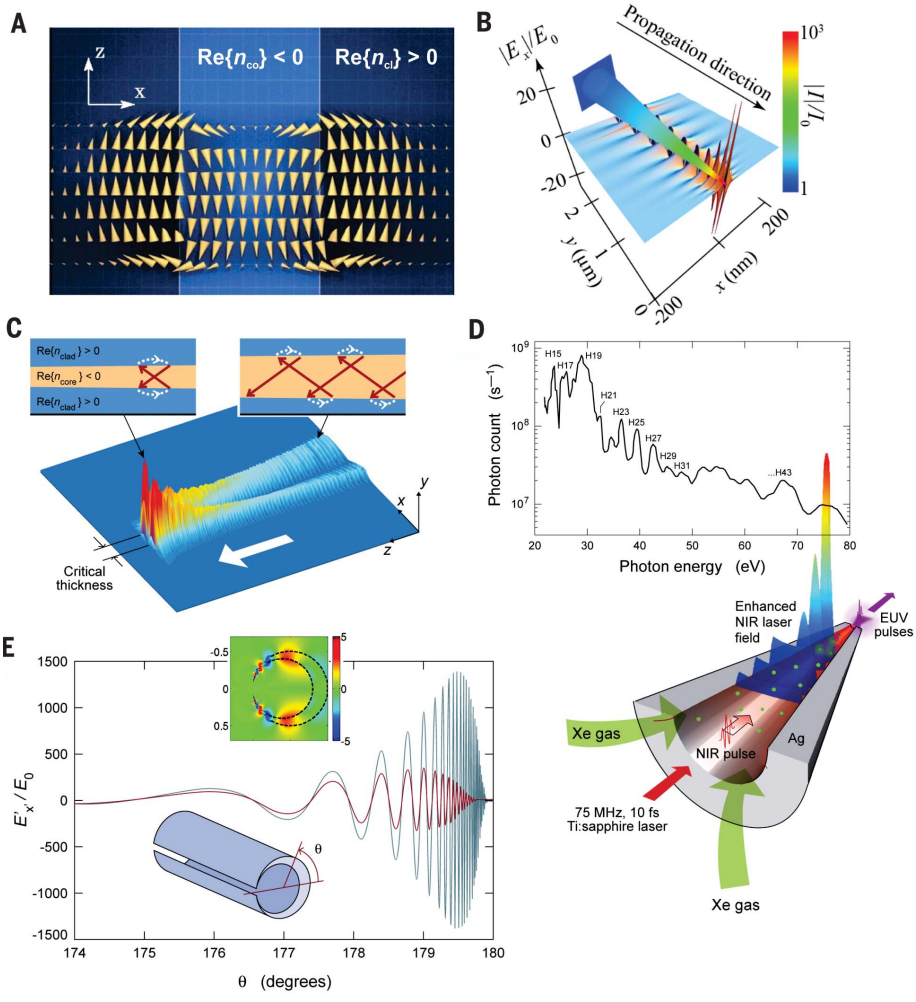

Fig. 1. Broadband ultraslow light in metamaterials and nanoplasmonics. (**A**) Structure of the Poynting vector field in a symmetric waveguide made of a negative–refractive-index core layer and positive-index claddings, showing the opposite directions of the power flux in the core ($P_{co} < 0$) and cladding ($P_{cl} > 0$) layers. Owing to the characteristic double-vortex structure of the power flux, the total time-averaged power flow in the $+z$ direction ($P_{tot} = P_{co} + P_{cl}$) is reduced, leading to correspondingly reduced energy and group velocities (*40*). (**B**) Adiabatic nanofocusing of surface plasmon polaritons (SPPs) guided along a tapered plasmonic nanoguide. The group velocity of the SPPs progressively reduces as they propagate, becoming zero at the nanostructure's tip, thereby leading to substantial spatial compression in the longitudinal direction and to a correspondingly large local field enhancement (here, of the order of ~10^3) (*41*). (**C**) Snapshot of the propagation of a monochromatic light wave along an adiabatically tapered waveguide with negative–refractive-index core and positive–refractive-index claddings. The light wave progressively slows down until it stops at a "critical" thickness, where the electric field builds up. The top-right and top-left insets associate the wave propagation with the corresponding zigzag ray picture at different guide widths. Note the negative Goos-Hänchen phase shifts (denoted with dotted white arrows) each time the ray hits an interface (*43*). (**D**) (Lower panel) A near-infrared (NIR, ~800 nm) SPP propagating along a tapered conical plasmonic nanoguide after being excited by a NIR laser pulse. The SPP slows down while propagating toward the exit aperture, where it eventually converges to a subwavelength high-intensity local spot. The hollow plasmonic (Ag) nanoguide is filled with xenon atoms, which are ionized by the high-intensity local field, producing high-harmonic extreme ultraviolet (EUV) pulses that are radiated through the exit aperture. The upper panel shows the measured high–harmonic-generation spectrum, spanning from the 15th to the 43rd harmonic (*68*). (**E**) Slow SPPs propagating azimuthally (in the θ direction) toward the singular ("kissing") point of the crescent nanostructure shown in the inset, after being excited by a plane wave. Shown is the amplitude of the x component of the electric field at an arbitrary 2D cross section of the nanocrescent. Note that the field-enhancement peaks at an angle other than 180°. The upper inset shows a cross-sectional plot of the amplitude of the x component of the electric field normalized by the incident field (polarized along x). The color scale in this inset is linear and restricted to [−5, 5], but the field magnitude is notably much larger around the singularity ("kissing point") of the two touching cylinders, as shown in the main figure (*64*).

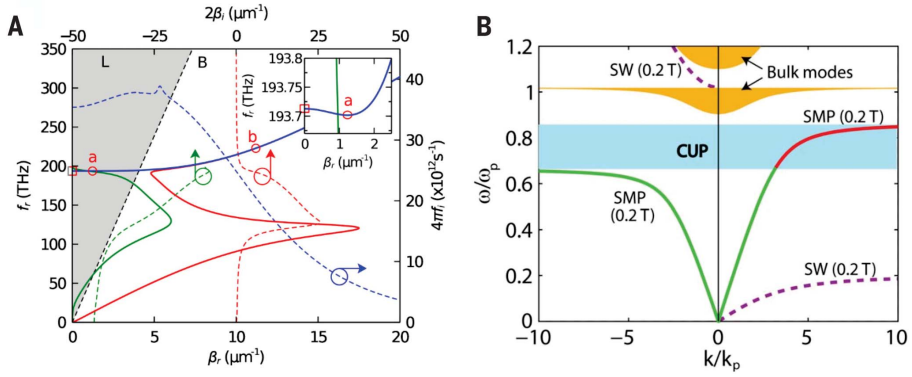

Fig. 2. Robust stopped light in the presence of absorption and scattering channels. In (A) and (B), the results displayed were obtained on the basis of exact, analytic solutions of Maxwell's equations. (**A**) Dispersion diagram of the two classes of complex TM_2 modes, complex-ω (blue) and complex-β (red and green), supported by a lossy plasmonic (ITO)–silicon–plasmonic (ITO) planar waveguiding heterostructure. Solid lines show the real part of the frequency [f_r = Re{ω}/(2π)] and of the longitudinal propagation constant (β_r = Re{β}), while the dashed lines show the corresponding imaginary parts (f_i = Im{ω}/(2π), β_i = Im{β}). The imaginary part of the frequency, f_i, provides the temporal losses associated with the complex-ω mode, while the imaginary part of the propagation constant, β_i, provides the spatial losses associated with the two complex-β modes. Note how only the complex-ω mode retains a zero group velocity, at point "a," where the band's slope locally becomes zero (see inset). The shaded gray region indicates the free-space light cone (*39*). (**B**) Band diagram of a gyroelectric-semiconductor (InSb)–silicon–plasmonic (Ag) heterostructure for the case where an external magnetic field B_0 = 0.2 T is applied in a direction perpendicular to the structure. Shown, both for positive and negative longitudinal wave vectors *k*, are the dispersion curve of the supported semiconductor–dielectric–metal surface magnetoplasmon (SMP), the surface wave at an InSb/Ag interface (SW), and the region of the bulk modes in InSb. The area shaded in cyan indicates the band region where complete unidirectional propagation (CUP) of the supported surface magnetoplasmon is attained (*69*).

with $\varepsilon_1 < 0$ and $\varepsilon_2 > 0$, but with $|\varepsilon_1| > \varepsilon_2$) (*45*, *46*). If κ is the component of the wave vector **k** perpendicular to the media interface, and γ is the decay constant of the field into medium "2," then the Goos-Hänchen phase shift is given by $\delta = 2\tan^{-1}[(\varepsilon_1\gamma)/(\varepsilon_2\kappa)]$ and becomes negative for $\varepsilon_1 < 0$ (and $\varepsilon_2 > 0$) (*43*). This negative phase shift—an interference effect of multiple "plane waves" into which the incident beam can be analyzed, each impinging on the interface with a slightly different angle of incidence—gives rise to a negative (backward) spatial displacement of the (center of the) beam, as shown schematically in the top insets of Fig. 1C. These backward "steps" in the propagation of a light ray along the guide can also be understood by comparison with the negative (backward) power flow in the core layer of the negative-index waveguide shown in Fig. 1A, and provide an intuitive, pictorial (yet accurate even at the level of Maxwell's equations) view of the light deceleration attained herein. These backward Goos-Hänchen steps arise from the presence of a bulk, volume-averaged negative refractive index or permittivity in one or more of the layers. As a result, the effect of possible bulk disorders and fluctuations in the layers of the heterostructure is naturally averaged out (contained in the definition of the macroscopic effective refractive index or permittivity) (*29*). It is only the negativity in the real part of the effective refractive index or permittivity that enables the deceleration of light, even in uniform structures containing layers made of completely amorphous (meta)materials (*44*). The associated structures may also be longitudinally uniform plasmonic media, where disorder is not an inherent issue. Detailed studies have shown that in the presence of nanometer-scale surface roughness, very large slowdown factors are still attainable—e.g., of the order of ~10^7 (*39*).

A universal characteristic of such negative-parameter wave-slowing structures—that one may also encounter for acoustic (*61*, *62*) ultraslow-wave structures and 2D materials—is that they allow for field accumulation and substantial field enhancement around the critical light-stopping point, deep below the diffraction limit, which can be exploited for a host of nanoscale applications. This is in contrast to, e.g., slow light in atomic media, where, although the energy density *U* is indeed enhanced in the slow-light regime ($U = P/v_g$, with *P* being the power density, and $v_g \to 0$), the electric-field amplitude *E* is not enhanced because most of the compressed energy is stored in the atomic polarization—and not in the electric field (*63*). Thus, although a light pulse is compressed in space (in the longitudinal direction of propagation) upon entering such an atomic ultraslow-light medium, and the energy density does increase, there is usually no enhancement in the local electric field.

The situation is different in the subdiffraction-limited nanophotonic structures considered here. Assuming a parabolic-like v_g profile with distance (with $v_g = 0$ at the critical point), it is straightforward to show that the time it takes for the light wave to exactly reach the critical point in an adiabatically tapered structure diverges logarithmically (*41*, *64*); hence, that critical point (where $v_g = 0$) is, in theory, never reached because the effective optical distance, Ln_g—where *L* is the guide's physical length—diverges ($n_g \to \infty$); it is as though a guided light wave propagates toward one end of an infinitely long waveguide (*65*–*67*), never quite reaching it. Accordingly, a sinusoidal light signal keeps accumulating, with a progressively smaller group velocity, near the "critical" zero-v_g point in this singular, idealized structure (Fig. 1, B and C). In practice, material imperfections lead to the critical point being reached, resulting in a back reflection, which together with material losses, provide a finite limit to how much the field can locally be enhanced. Nevertheless, the large spatial compression of the field in the slow-light regime of such subdiffraction nanostructures leads to correspondingly large field-enhancement factors—of the order of 350 or more—being realistically attainable, and over ultrabroad bandwidths [e.g., full width at half maximum (FWHM) of 100 nm in the near-infrared] (*68*). The back reflection can be rigorously suppressed if nonreciprocity is broken, e.g., by application of a magnetic field in gyroelectric semiconductors (such as InSb) (*55*, *56*, *69*) or by deploying PT-symmetric structures (*58*), in which case rigorous light-stopping can be obtained. The ultimate degree of slow-light–aided field enhancement is set by the nonlocal effects in plasmonic structures and by the size of the unit cells in metamaterial structures (spatial dispersion), which limit how much a light field can be spatially compressed (*70*–*72*). These nonlocal (spatial dispersion) effects usually arise at scales less than ~1 to 5 nm (~30 to 50 nm), and in that deep-subwavelength regime, the induced spatial frequencies (i.e., wave vectors) are large, to the point of potentially allowing for "direct diagonal" *s*-band absorption (i.e., Landau damping) (*32*)—thereby potentially providing an additional loss channel that should be avoided. Such "structural slow-light" field enhancements are also obtained in photonic structures above the diffraction limit, as in photonic crystals and coupled-resonator optical waveguides (*4*–*6*, *21*–*28*). However, the compression and focusing of light in those cases is limited by the wavelength of light and cannot reach the truly nanoscopic dimensions (and corresponding nanoscale applications) targeted herein.

Robustness in the presence of dissipative and scattering channels

A key issue to be addressed when attempting to slow down or stop guided light signals in nanoscale structures is how dissipative losses (*39*, *49*–*53*) and back-scattering channels (*54*–*56*, *69*) might affect the light-deceleration ability of these devices. Because the slowing-down of light is due to the presence of negative electromagnetic parameters (Fig. 1, A to C), which normally entail losses and dispersion, the modes of these structures will in general be complex (*53*), and it is important to examine whether the zero-v_g points in the associated dispersion diagrams are still preserved

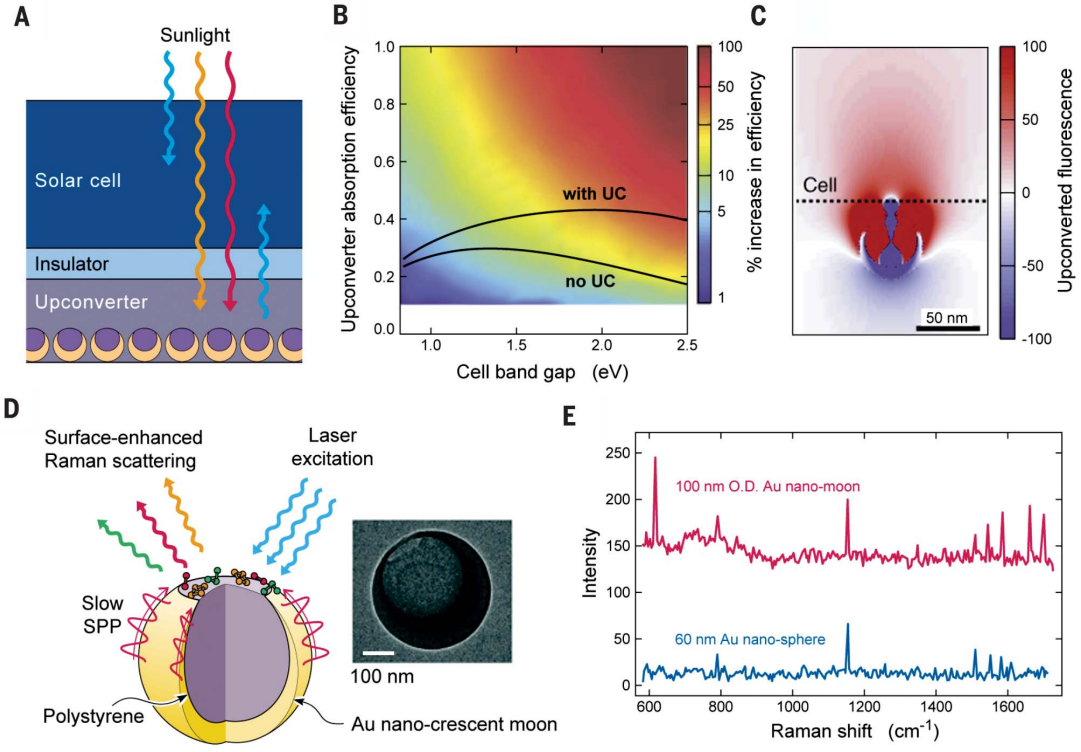

Fig. 3. Broadband ultraslow light at the meta-atomic level, and its application in photovoltaics and biosensing. (**A**) Schematic illustration of a solar cell based on an upconverter system where above-bandgap light is absorbed by the cell, while sub-bandgap light is initially absorbed in the upconverter layer, converted to above-bandgap light, and sent back to the cell where it is harvested. The upconverter consists of slow-light nanocrescent meta-atoms, whose core is doped with the upconverting material (*86*). (**B**) The upconverter substantially increases the efficiency of an ideal single-junction solar cell. As shown, the relative increase is greatest when the upconverter absorption efficiency and the cell bandgap are high. The black-line inset shows the absolute efficiency of an ideal solar cell, both with and without an ideal upconverter (UC) (*86*). (**C**) Calculation of the upconverted power toward the solar cell (in W/m^2). At a wavelength of 644 nm, the power flow into the cell is enhanced by more than 100 times compared with the case (not shown here) where there is no crescent in the upconverter (*86*). (**D**) Conceptual illustration of a SERS substrate made of broadband slow-light nanocrescent moons. The gold surface is functionalized with biomolecular linkers to recognize specific biomolecules. Also shown on the right is a transmission electron microscope image of an actual nanocrescent moon, with an inner diameter of 300 nm and a bottom thickness of 100 nm (*87*). (**E**) Comparison between the SERS spectra of 1 mM R6G molecules sitting on top of the slow-light nanocrescent moons and on 60-nm standard colloidal Au nanospheres (*87*).

when Joule losses are present. Furthermore, because the light-stopping points are usually reached and accessed with an adiabatic taper (Fig. 1, B and C), it is also crucial to check whether the taper might introduce back-scattering channels through which the trapped (stopped) light energy might escape.

Both of these issues have been extensively investigated and addressed. Exact solutions to Maxwell's equations in lossy plasmonic-dielectric-plasmonic heterostructures (*39*) reveal that there are two classes of modes in these structures (*39*, *49*–*53*) (Fig. 2A). The first class is characterized by a real frequency f and complex longitudinal wave vector $\beta = \beta_r + i\beta_i$ (red and green lines in Fig. 2A), and does not preserve the zero-v_g points in the presence of losses (*49*). These modes can be excited by sinusoidal steady-state sources because they are characterized by a well-defined real frequency (and complex wave vector owing to the losses). They are not the modes of interest in the stopped-light regime, because in that regime where light is trapped, spatial losses (complex wave vectors) lose their physical meaning (*53*)—a stopped light pulse simply decays with time at its localization point, rather than decaying in space (because it does not propagate); hence, spatial losses and the search for complex-β solutions cease to be physically meaningful in the stopped-light regime. The second class of modes, by contrast, is characterized by a complex frequency $f = f_r + if_i$ and real longitudinal wave vector β (blue lines in Fig. 2A) (*39*, *51*–*53*). These "complex frequency" modes are somewhat similar to modes excited inside lossy cavity resonators and are the ones to be sought after in the stopped-light regime. They can be excited by short pulses that, e.g., have f_r as their central frequency and a bandwidth (*38*) $\Delta\omega = f_i$. Notably, the temporal losses characterizing these modes increase by only a small factor when entering the stopped-light regime (e.g., from ~2.4 × 10^{13} s^{-1} at point "b" to ~3.6 × 10^{13} s^{-1} at the zero-v_g point "a" in Fig. 2A, an increase by a factor of only 0.5—and corresponding to lifetimes at the stopping point of ~30 fs, which are typical nanoplasmonic ones) (*39*, *51*–*53*).

A forceful way to solve the second potential issue and suppress back-scattering channels is to induce a unidirectionality mechanism, e.g., either by application of a static magnetic field in gyroelectric or gyromagnetic structures (*55*, *56*, *69*), nonlinear or refractive-index modulation mechanisms (*57*), PT-symmetric media (*58*), or photonic topological insulators (*59*, *60*). For instance, Fig. 2B shows that the first of the aforementioned schemes, when applied to a (gyroelectric) semiconductor-dielectric-metal heterostructure, leads to a region in the band diagram where complete unidirectional propagation (CUP) is allowed. A guided pulse with a bandwidth falling inside this CUP region can neither scatter to backward modes ($k < 0$ in Fig. 2B) nor to bulk modes in the semiconductor (orange-colored regions in Fig. 2B) nor to surface waves (SWs) at the semiconductor-metal interface of such a metal-terminated waveguide—nor can it be perturbed by surface roughness and geometric imperfections, given that it is a photonic analog of a quantum Hall state (*55*, *69*). Thus, with such unidirectional schemes suppressing back-scattering channels, robust slow and stopped light can be attained, unaffected by spatial variations in the guiding structure.

Applications of subdiffraction ultraslow light and acoustic waves

An example of such a broadband ultraslow-light effect, below the diffraction limit, and its application is illustrated in Fig. 1D, where an adiabatically tapered plasmonic nanoguide capable of decelerating and accumulating at its tip SPPs over a broad band (~100 nm) (compare Fig. 1B) is used as a means of generating ultrashort, extreme-ultraviolet (EUV) pulses from near-infrared incident pulses (centered at ~800 nm) (*68*). The SPPs in this tapered hollow nanocone

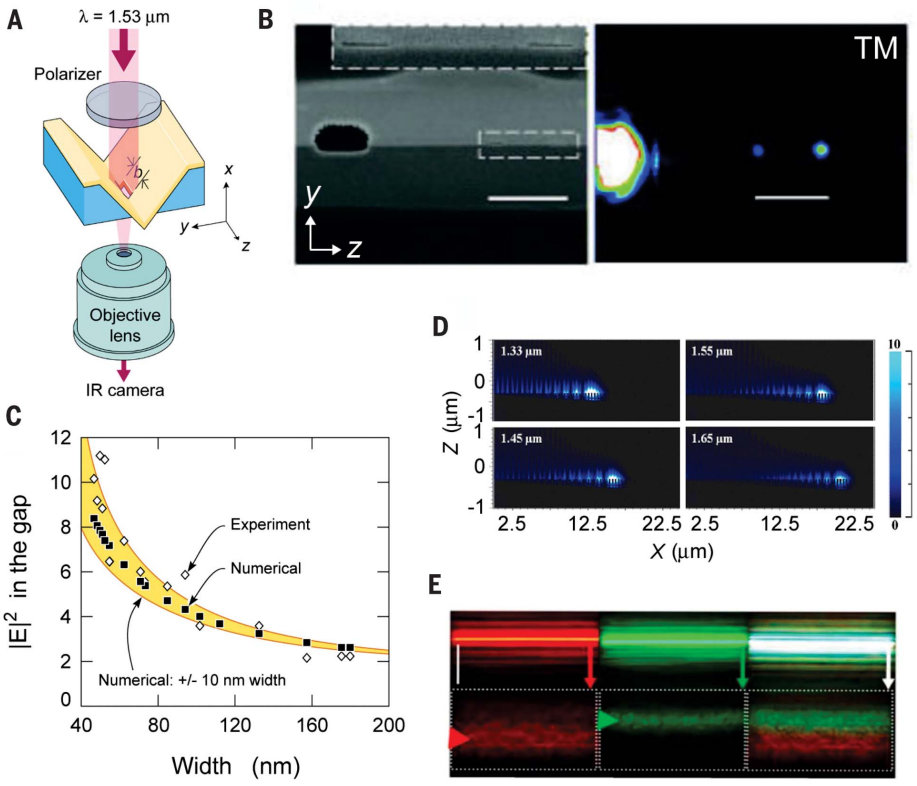

Fig. 4. Broadband slow, conventional and "spoof" surface plasmon polaritons, and their application in spectrum demultiplexing and color sorting. (**A**) Schematic illustration of the experimental setup used for slowing and bringing to the nanoscale TM-polarized light (magnetic field parallel to the *z* axis). The incident vacuum wavelength was 1532 nm (*80*). (**B**) (Left) An SEM image of two subwavelength-width (~100 nm) V-groove output slits and a large reference hole as seen from the back side (along *x*). (Right) Output signal for TM polarization of the incident lightfield. When the incident-light polarization is transverse electric, no plasmon mode is excited at the two subwavelength slits (*80*). (**C**) Dependence of intensity ($|E|^2$) enhancement with the width of the V-groove slit, as determined experimentally and numerically (*80*). (**D**) Numerical simulations of slow "spoof" SPPs propagating along a tapered plasmonic grating. SPPs of broadly different frequencies (in the telecommunications regime) are stopped and trapped at correspondingly different points along the nanoguide (*76*). (**E**) Experimental demonstration, at visible frequencies, of the scheme in (D). Here, visible light of different colors is incident on a nanoslit from the bottom of the structure (the nanoslit extends horizontally, and is perpendicular to the arrows at their starting points), acquiring enough momentum to couple to spoof SPPs. The SPPs excited in this way propagate slowly in the direction indicated by the arrows along the tapered grating (shown here from above), with each color eventually being stopped and trapped at a different groove depth ("rainbow trapping"). The white scale bar shown in the top left panel corresponds to 10 μm (*97*).

are markedly slowed down near its exit point, accumulating in an area with a diameter of ~240 nm. Atomic gases enter the device at the input port and are controlled by changing the pressure between the input and output ports. Despite the plasmonic losses, optimized structures lead to intensity enhancements exceeding 20 dB (i.e., a factor of ~350), enough to trigger atomic ionization with moderate input intensities of ~1×10^{11} W cm^{-2}. This leads to high-harmonic generation, up to the 43rd harmonic (Fig. 1D) and deep into the UV regime (photon energy ~67 eV). In addition to not requiring phase matching, as the field concentration is deep-subwavelength, an advantage of this means of nanolocalizing and enhancing the intensity of light compared to bowtie or nanorod elements is that the large field enhancements occur over substantially larger nanovolumes (with a diameter of ~240 nm and a length of ~450 nm), thereby enhancing the efficiency of the nonlinear generation. For instance, the photon number measured for the 15th and 17th harmonics was ~1×10^9 photons/s, corresponding to a conversion efficiency of ~1×10^{-8}, which is about 10 to 100 times higher than that measured for a 150-bowtie-nanoantenna array (*73*). We note that under similar conditions, noncoherent multiphoton or high-field fluorescence may also dominate the spectra (*74*), because these effects too are favored below the ionization threshold by the large field enhancements and the linear interaction-length scaling.

This type of broadband slow-light structure need not be planar (*39*, *65*–*67*) or linearly tapered (*41*–*43*, *73*–*82*), with two examples being the cylindrically (*64*) or spherically (*83*) crescent nanostructures (Figs. 1E and 3). Surface plasmon modes excited by a uniform electric field of wavelength λ ~375 nm travel with a gradually slower speed toward the singular "kissing" point of the two cylinders (of external radius ~20 nm) where they accumulate, having a gradually smaller wavelength and increased energy density (Fig. 1E). On the basis of a transformation-optics analytic approach, it was shown that this effect is ultrabroadband—across the entire visible spectrum—and, despite the plasmonic loss, leads to large field enhancements, of the order of 10^3, at the critical stopping point (*64*). The role of surface roughness and unavoidable geometric bluntness and imperfections has also been studied (*84*, *85*), and it was found that the structures' fundamental behavior remained unaltered. We note that similar plasmonic nanostructures have been reported, even ones with subnanometer features, in the regime where nonlocal effects start playing a dominant role (*70*–*72*).

An example of how such a broadband slow-light–aided field enhancement can be exploited to improve the performance of photovoltaic solar cells is shown in Fig. 3A. A layer containing spherical nanocrescents composed of an upconverter-doped dielectric core and a crescent-shaped metallic shell is placed behind the solar cell (*86*), capable of transforming over broad spectral and spatial regions transmitted low-energy photons to higher-energy, above-bandgap photons that can be absorbed by the solar cell. Detailed calculations showed a 100-fold increase in above-bandgap power emission toward the solar cell (*86*) and a greater than 10-fold absorption enhancement for a broad range of sub-bandgap wavelengths (Fig. 3, B and C), leading to single-junction solar cell power-conversion efficiencies that can exceed the Shockley-Queisser limit (from ~30 to >44%). Such nano-engineered structures provide one with the ability to exploit broadband slow-light and large near-field intensity-enhancement effects right at the meta-atomic level, i.e., not only the macroscopic overall structure but also its constituent metamolecules (nanoantennas) can be designed to harness broadband slow light—a unique feature compared with other macroscopic slow-light-structure designs.

These slow-light "nanocrescent-moon" metamolecules can also be used as an ultrasensitive surface-enhanced Raman scattering (SERS) substrate (Fig. 3D) (*87*). The gold nanocrescents (300-nm inner diameter and 100-nm bottom thickness) are functionalized with biomolecular linkers to identify specific biomolecules. When a single gold nanocrescent moon is excited by a 785-nm diode laser, the broadband hotspot that is generated is used to detect the SERS spectra of rhodamine 6G (R6G) molecules, with an enhancement factor larger than 10^{10}. Comparing the SERS spectra of 1 mM R6G molecules on a single gold nanocrescent moon and on 60-nm colloidal nanospheres (Fig. 3E) shows substantial improvement when the former structure is used—both in the number and the relative intensity of

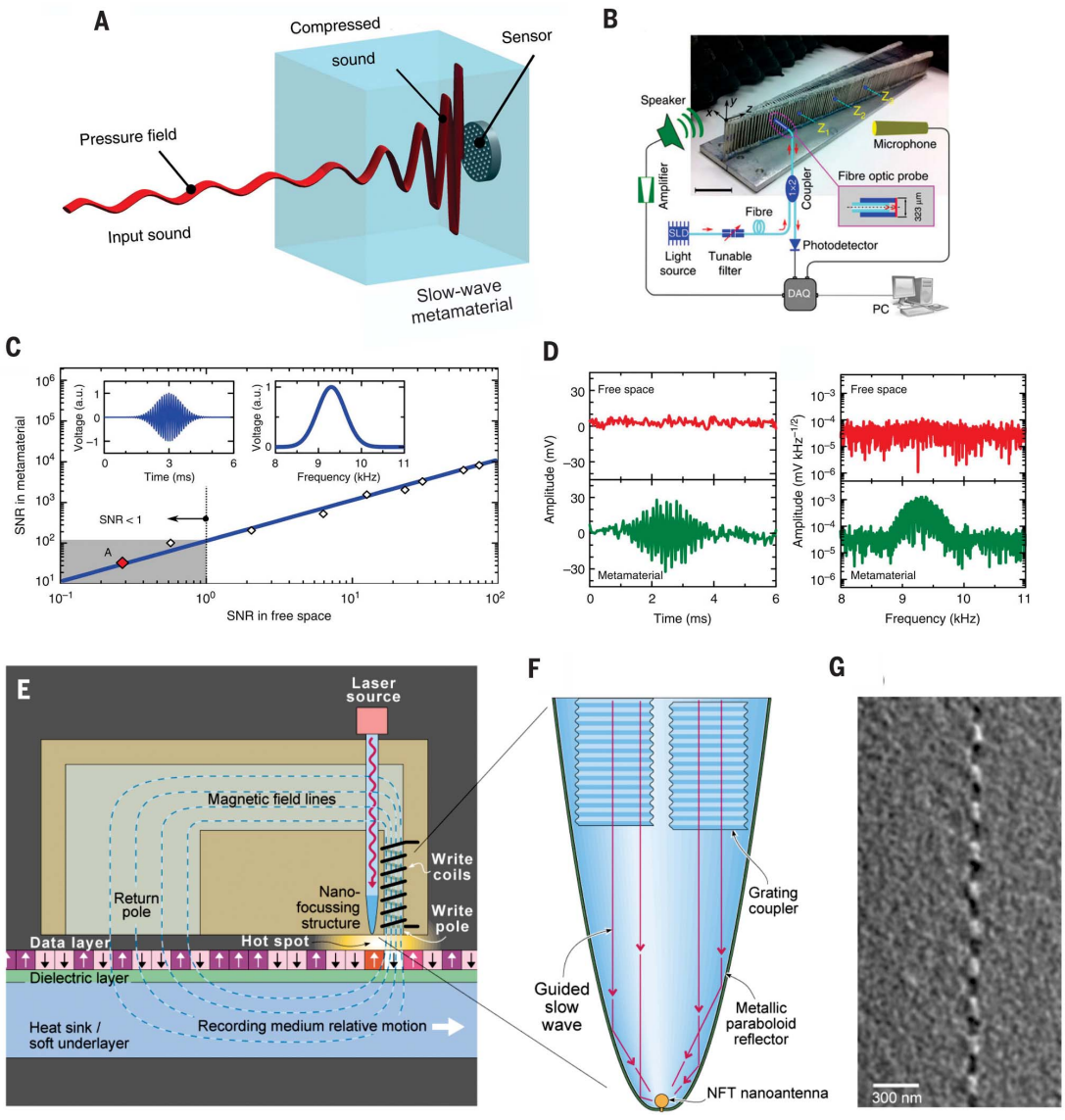

Fig. 5. Adiabatic wave slowing-down and focusing for enhanced acoustic sensing and nanooptical heat-assisted magnetic recording (HAMR). (**A**) Schematic of how the pressure field of a sound wave is spatially compressed and enhanced while decelerated inside an acoustic metamaterial, before being detected by a sensor (*61*). (**B**) Photonic-acoustic metamaterial hybrid sensing system. The device is constructed from an array of stainless-steel plates, spaced by air gaps, and has a progressively increased width (*61*). (**C**) The signal-to-noise ratio (SNR) measured in the metamaterial compared with that obtained in free space. The inset shows the input Gaussian pulses from the speaker in time domain (left) and frequency domain (right). The diamonds are the experimental data and the solid line is the fitted curve with a slope of 114, indicating an ~20-dB SNR improvement by using the ultraslow–acoustic-wave–enhanced sensing system. In the gray highlighted zone, the measured free-space SNR is smaller than 1, indicating that the input signal is below the detection limit (*61*). (**D**) Time-domain and frequency-domain pulse signal measured in free space (top) and in the metamaterial (bottom). The SNR measured in the metamaterial device is 32.7, compared with the measured free-space SNR of 0.27, which corresponds to point A in (C) (*61*). (**E**) A HAMR head records data to a disk medium of high thermal stability. Here, a guided wave excited by a laser source propagates slowly along a parabolically tapered metal-clad waveguide [shown in (F)], adiabatically stopping and focusing at the cutoff-tip of the guide, and eventually coupling to a judiciously shaped plasmonic nanoparticle (nanoantenna). The wave's adiabatic slowing and stopping is similar to that shown in Fig. 1, B to E, and Fig. 3, A and D, but for a parabolic taper. The resulting high-intensity local field is used to heat the recoding medium locally, assisting the recording process by temporarily lowering its resistance to magnetic polarization (*101*). (**F**) Schematic illustration (not to scale) of a side view of the HAMR recording head. In the upper part of the recording head, a grating couples laser-diode light to the parabolically tapered metal-clad optical waveguide. At the bottom of the tip, there is a plasmonic nanoantenna ("near-field transducer," NFT) on which light energy is evanescently coupled (red arrows) (*101*). (**G**) Magnetic force microscope image of a recorded track. The track width is ~70 nm (scale bar, 300 nm) (*101*).

the resolved Raman peaks. These broadband slow-light nanophotonic crescent moons exhibit Raman enhancement factors (for an 830-nm laser excitation source) exceeding 10^{10}, as compared with 10^{3} to 10^{4} for on-resonance Au nanospheres (using 514-nm laser excitation) reported previously (*88*).

The broadband field-enhancement in the ultraslow-light regime of tapered metamaterial and nanoplasmonic waveguides has been exploited in a variety of further applications, including broadband thin-film infrared absorbers (*89*), spontaneous-emission enhancement of single quantum dots and nonclassical light sources (*90*), cavity-free stopped-light nanolasing, and active on-chip nanophotonic devices (*34*, *91*–*94*). However, several of the reported 3D subdiffraction slow-light structures, such as the linearly tapered cylindrical nanoguides in Fig. 1, B and D, are standalone devices, with a challenging on-chip implementation. A first quantitative study toward overcoming this issue was reported in (*80*), which demonstrated nanoscale 2D slowing of light in the form of SPPs (Fig. 4, A to C). Here, light was adiabatically slowed down and squeezed (with an efficiency of ~50%) through a 45 nm by 2 μm V-groove slit aperture, resulting in a measured intensity enhancement of ~10—the defining feature of so called "structural slow light" (*4*–*6*) in guiding structures, both below and above the diffraction limit. The full extension of this nanoscale slow-light scheme to three dimensions was reported recently (*95*), giving rise to experimentally estimated intensity enhancements of ~400 within a mere 14 nm by 80 nm cross-sectional area and allowing for efficient on-chip slow light that can be readily integrated with

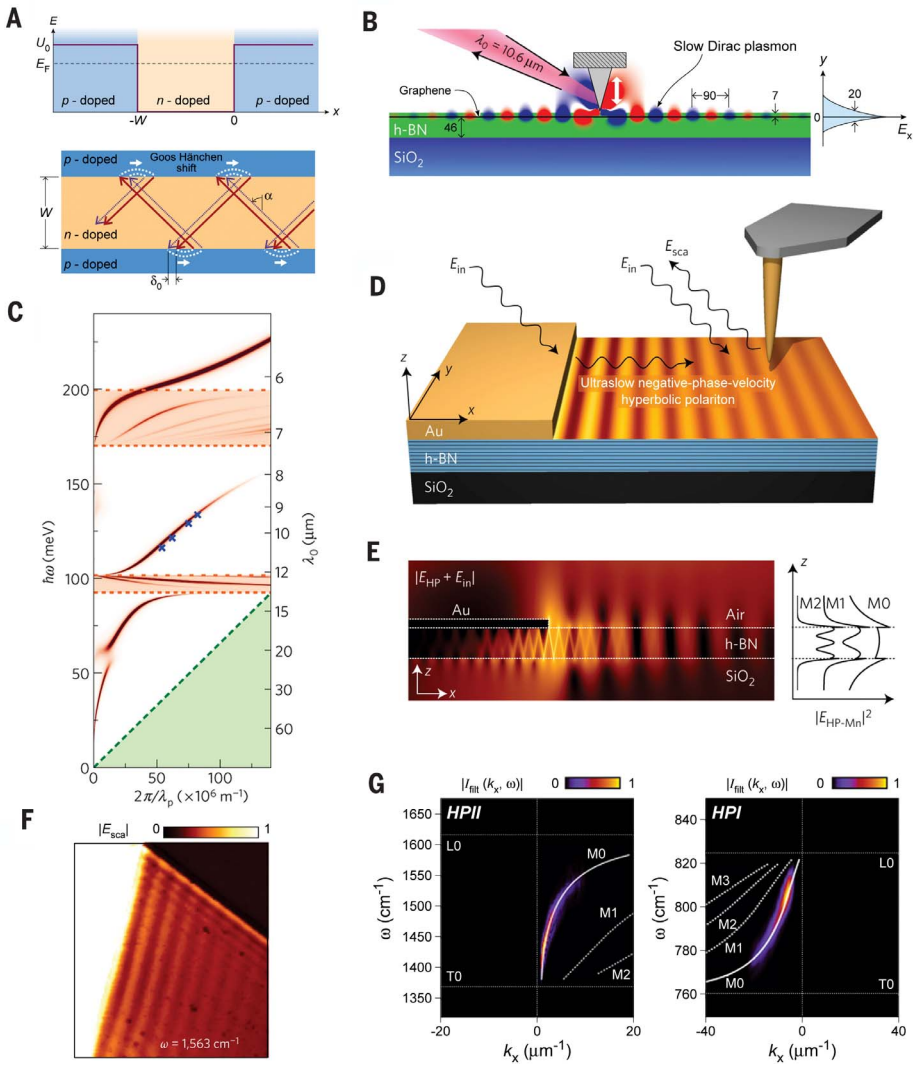

Fig. 6. Broadband ultraslow guided Dirac electrons, plasmons, and phonon-polaritons in graphene, van der Waals crystals, and heterostructures. (**A**) (Top) Potential profile of n-doped graphene, bounded symmetrically by two p-doped regions. (Bottom) Illustration of the reflections of the two pseudospin Dirac-electron components at the two p-n interfaces, along with the associated negative quantum Goos-Hänchen phase shifts. The two zigzag-propagating rays, shown in red and purple, trace the movement of the center of a guided slow electron beam on the two graphene sublattices (*102*). (**B**) Schematic of graphene encapsulated by h-BN, and the associated s-SNOM measurement setup for the excitation of a guided slow Dirac plasmon. The simulated E_x field-component of the plasmon in the out-of-plane direction (20 nm full-width at half-maximum) is shown on the right (*104*). (**C**) Calculated dispersion diagram of the slow Dirac plasmons of (B), for a carrier density of $n_s = 7.4 \times 10^{12}$ cm^{-2}. The crosses show experimental data, and the shadowed regions show the h-BN frequency bands where propagating phonon polaritons can exist (shaded orange) and the electronic intraband Landau damping region (shaded green). The red background color shows the imaginary part of the reflection coefficient of evanescent waves, evaluated at the top h-BN surface using the transfer-matrix method for a vacuum–SiO_2(285 nm)–h-BN(46 nm)–graphene–h-BN(7 nm)–vacuum heterostructure (with the dips in the reflection coefficient coinciding with the excited modes in the heterostructure) (*104*). (**D**) Schematic of structure and the setup for exciting and observing ultraslow negative–phase-velocity hyperbolic phonon polaritons in a thin h-BN slab. The polaritons are launched with the aid of the metal (Au) edge, and the thickness of the h-BN layer is 135 nm. Type I polaritons are found in the spectral region 22.8 THz (13.6 μm) to 24.7 THz (12.1 μm), whereas type II polaritons exist between 41.1 THz (7.3 μm) and 48.3 THz (6.2 μm) (*109*). (**E**) (Left) Numerical calculation of the field distribution (on a logarithmic scale) for the structure of (D), at ω = 1563 cm^{-1} (46.9 THz; 6.4 μm). The propagation of the type II fundamental hyperbolic polariton mode is shown as rays propagating in a zigzag fashion along the slab, being reflected from the top and bottom media interfaces—similarly to the zigzag ray propagation shown in Fig. 1C (although here the phase velocity of the type II mode is positive and the Goos-Hänchen phase shifts are not clearly discerned). (Right) Field-intensity profiles of the first three guided hyperbolic slow modes (*109*). (**F**) Infrared near-field image of the interference between the polaritons launched by the gold edge and those by the tip [see (D)] upon being reflected by the h-BN edge (*109*). (**G**) Comparison between the experimentally (color) and numerically (white solid) determined dispersion curves of the fundamental type II (left) and type I (right) hyperbolic polariton mode. The white dashed lines show numerically calculated higher-order guided modes (*109*).

other on-chip nanophotonic components. The spatial compression achieved in the slow-light regime of plasmonic slot nanoguides was exploited in (*95*) to reduce the length and overall footprint of a plasmonic electro-optic phase modulator (*96*), giving rise to large bandwidths (~120 nm around 1.55 μm), high modulation speeds (~40 Gbit s^{-1}), compactness (a length of only ~29 μm and a width of ~140 nm), and energy-efficient operation (energy consumption ~60 fJ bit^{-1}).

This type of ultrabroadband light deceleration can be attained in almost any regime of the electromagnetic spectrum, from microwaves (*66*, *67*) to the terahertz (*55*, *75*, *77*), near-infrared (*76*), and visible regime (*78*–*82*, *97*, *98*), using suitably engineered plasmonic structures. Two examples of this are shown in Fig. 4, D [theory, at telecommunication wavelengths (*76*)] and E [experiment, at visible wavelengths (*97*)]. Figure 4E shows so-called "spoof" (engineered) SPPs being excited at a nanoslit (extending horizontally, from left to right, in the upper panels, perpendicularly to the arrows) and propagating along the direction of the arrows. The SPPs propagate along a tapered plasmonic grating structure, similar to that discerned in Fig. 4D, in the direction indicated by the arrows. In this adiabatically tapered structure, the period and the width of the grooves are fixed (~475 and 150 nm, respectively), but the groove depth increases with distance slowly from ~6 to 100 nm. As they propagate along the adiabatically tapered structure, the SPPs (in the visible-wavelength region, 500 to 700 nm) disperse, with each visible color eventually being trapped and localizing at a correspondingly different point along the tapered structure—with the larger (red) wavelengths localizing at the deepest grooves. These experimental results, therefore, provide confirmation in the visible regime of the spatial demultiplexing and trapping at different positions of the spectrum of a broadband pulse ("rainbow trapping") propagating along a tapered plasmonic waveguide—similar to the effect outlined theoretically in Fig. 1, B

and C, for tapered plasmonic and negative-index waveguides, respectively. The resulting spectrum demultiplexing can, in this scheme, find interesting applications for on-chip spectroscopy (*82*), filtering, and color sorting (*78*, *99*).

As an essentially interference phenomenon (Fig. 1, A and C), the wave deceleration in adiabatically tapered metamaterial waveguides can also be exploited for acoustic waves (*61*, *62*). Here, the concept of metamaterials (judiciously engineered media with desired wave responses) is especially fitting as it allows the design—in the deep-subwavelength, true–effective-medium regime—of structures with broadband slow-wave acoustic responses that are unattainable with natural media. An example is illustrated in Fig. 5, A to D. Here, a tapered acoustic metamaterial waveguide brings an input pressure field (sound wave) to a halt at a critical point inside the waveguide, where the acoustic field can then build up and be locally enhanced (compare Fig. 1, B and C, for the photonic analog), so that it can be detected with ultrahigh sensitivity by an acoustic sensor at the guide's end (Fig. 5A) (*61*). The acoustic-metamaterial device is constructed by an array of stainless plates, spaced by air gaps, and behaves as a continuous medium. Excited by a speaker, the acoustic wave (frequency ~7 kHz) propagates with a progressively slower speed along the structure, and is therefore spatially compressed and enhanced in amplitude, until it is eventually detected at its stopping point by a fiber-optic microphone integrated at the wide, open end of the device (Fig. 5B). More than 10-fold pressure amplification is achieved in this way. The broadband acoustic-wave enhancement in this type of a system is so large that it can be used to successfully recover very weak acoustic-pulse signals far below the detection limit of conventional acoustic-sensing systems. Figure 5, C and D, shows how a series of Gaussian-modulated acoustic pulses with a center frequency of 9.3 kHz and a bandwidth of 0.5 kHz are effectively amplified in the slow-wave acoustic-metamaterial device, with a signal-to-noise ratio (SNR) enhanced by more than 100 times (that is, more than 20 dB) compared with that obtained in free space. This SNR enhancement enabled the metamaterial slow-wave system to detect weak acoustic signals below the detection limit of a conventional acoustic sensor. Indeed, Fig. 5D (top) shows that whereas the measured free-space signal is completely overwhelmed by the noise (i.e., SNR = 0.27), the same weak acoustic pulse is successfully recovered (i.e., SNR = 32.7) in the slow-wave metamaterial region (Fig. 5D, bottom).

Finally, Fig. 5, E to G, highlights what we believe is one of the most exciting and technologically promising applications of slow-light–aided nanoscale field-enhancement: heat-assisted magnetic recording (HAMR) for data storage. Since 2012, the density growth rate of hard disk drives (HDDs) has begun saturating owing to fundamental physical limits reached by perpendicular magnetic recording—in particular, because the required writing field in HDD electromagnets must be higher than that of the magnetic flux saturation in a typical CoFe-based electromagnet (*100*). A promising avenue that the industry is currently pursuing to overcome this limitation is HAMR, which exploits the sudden drop of a magnet's coercivity at the critical Curie temperature. To achieve the required high local heating (~400°C), typically ~80 μW of laser light from an inexpensive semiconductor diode (operating at ~830 nm, although blue-ray laser diodes can operate at ~400 nm) must be efficiently brought to the nanoscale to heat (from only ~5 nm above the recording head) a volume of ~50 nm by 15 nm by 10 nm of a FePt ferromagnet. To put this into a context, the required power density for HAMR is ~1000 times larger than that resulting from standard Au-coated tapered optical fibers used in near-field scanning optical microscopy (NSOM), which typically have an optical transmission efficiency of less than 10^{-5}. Figure 5, E and F, shows an example, reported in 2009 by Seagate Technology, of how slow-light nanoguides can be used in a HAMR recording head to solve the above challenges (*101*). Here, diode-laser light at 830 nm is coupled to a gold-coated parabolically tapered Ta_2O_5 slab. As it propagates along the metal-clad tapered waveguide (*45*), the light signal is gradually decelerated, spatially compressed, and enhanced in amplitude, until it reaches the guide's cutoff thickness where it momentarily stops [$v_g = 0$ at the cutoff (*45*)]—a behavior fundamentally similar (*64*, *83*–*85*) to that described for the structures of Figs. 1 and 3, except that the taper is not linear (Fig. 1, B and D), cylindrical (Fig. 1E), or spherical (Fig. 3, A and D) but rather parabolic. It then evanescently couples with good efficiency to a gold nanoantenna, producing an intense localized field, well below the diffraction limit, and only a few nanometers above the hard disk—enough to induce the required local heating. For optimized structures, Challener *et al.* (*101*) reported maximum field-enhancements of ~2000, and a maximum coupling efficiency (at ~870 nm) of ~8%—orders of magnitude greater than the coupling efficiency of conventional apertures with diameters of the same dimensions as the nanoantenna. This method has thereby enabled local heating of a magnetic track only ~70 nm wide (Fig. 5G), giving rise to a data-recording areal density of ~375 Tb m^{-2}—much higher than previously reported storage densities (*100*, *101*). Important remaining challenges for this technique concern the efficient integration of materials that will be even more resilient to thermal damage (upon repeated heating cycles), more efficient heat sinks, and dedicated nanometer-gap–regulation techniques between the writing head and the recoding disk.

Broadband ultraslow electron and phonon-polariton waves in 2D materials

The nonresonant mechanisms for the deceleration of guided light waves in nanostructures containing media with negative optical parameters (Fig. 1, A to C) also play a critical role in the slowing-down of electron and phonon-polariton waves in 2D nanoguides and heterostructures. Here, an additional advantage is the convenience with which one can control the velocity of guided matter waves, e.g., by smoothly varying a gate voltage applied on a 2D graphene quantum-well structure, thereby allowing for the possibility of variable delays—an important aspect of coherent buffers and memories (*4*–*6*).

The quantum Goos-Hänchen effect in the ultrarelativistic limit of massless electrons, relevant for graphene, considered the propagation of massless spin-½ particles in two dimensions, in a p-n-p single-layer graphene junction with a voltage (potential barrier) U_0 applied in the p-doped regions (*102*) (Fig. 6A, upper panel). It was found that the Goos-Hänchen effect at the p-n interfaces depends on the pseudospin (sublattice) degree of freedom of the massless Dirac fermions, and, moreover, that it changes sign at an angle of incidence $\alpha_s = \arcsin\{(\sin\alpha_c)^{1/2}\}$, where α_c is the critical angle for total reflection, for Fermi energies $E_F < U_0$. For angles of incidence smaller than α_s, the shift becomes negative (Fig. 6A, lower panel), just as with guided light waves in metamaterial and plasmonic waveguides shown in Fig. 1C. In that regime, the group velocity v of the guided quasiparticles can become zero. In particular, as the normalized width ($U_0W/\hbar v$) of the central n-doped channel is progressively reduced to around unity, i.e., as one enters the full quantum-mechanical regime, the dispersion relation of the lowest channel mode features two pronounced minima (where the group velocity reduces to zero, $v = 0$), each contributing to the conductance a quantum of $e^2/\hbar$ per spin and valley degree of freedom, thereby making a total contribution to the conductance of $8e^2/\hbar$—a macroscopic conductance step that is observable in these bipolar junctions. Similar effects can be observed in bilayer graphene junctions, too, where it is possible to coherently decelerate, stop, and reaccelerate the guided quasiparticles, allowing for interesting coherent-manipulation functionalities in graphene-based integrated devices (*103*).

In addition to slowly propagating guided Dirac fermions in doped graphene slots of suitable geometry, there is currently much interest in the interaction of infrared light with Dirac plasmons or phonons, particularly in the slow-wave regime of these nanostructures. In this regime, the longitudinal wave vector of the guided wave is large and the effective wavelength small, leading to volume confinements that can be millions of times smaller than in free space, with relatively low losses—thereby allowing for ultrastrong light-matter interactions. An interesting example of this is illustrated in Fig. 6B, which shows a graphene sheet encapsulated by two films of hexagonal boron nitride (h-BN)—the whole structure assembled by a polymer-free van der Waals (vdW) assembly technique (*104*, *105*). Hexagonal boron nitride is an interesting optical material for nanoscale slow-light applications as it exhibits natural hyperbolic behavior (*106*), i.e., the in- and out-of-plane components of the permittivity tensor have opposite signs in the reststrahlen frequency bands. Figure 6C

presents the dispersion diagram (energy/wavelength versus wave vector) of propagating Dirac plasmon modes in the structure shown in Fig. 6B. In Fig. 6C, the crosses are the experimentally extracted data, indicating group velocities $v_g = (\mathrm{dRe}q_\mathbf{p}/\mathrm{d}\omega)^{-1}$, with $q_\mathbf{p}$ being the plasmon wave vector, as small as ~10^6 m s^{-1} (group refractive index ~300), and corresponding to observed lifetimes (not shown directly in this figure), $\tau_\mathbf{p} = (\mathrm{Im}\, q_\mathbf{p})^{-1}/v_g$, as long as ~500 fs (*104*)—more than an order of magnitude longer than those of pure surface plasmons in silver, which are typically ~20 fs (*36*). Furthermore, the wavelength $\lambda_\mathbf{p}$ of the Dirac plasmons is as low as 70 nm—~150 times smaller than the free-space wavelength of the incident light. With an even further improvement of these plasmons' lifetimes, such a structure should be ideal for slow-wave applications where ultrahigh field confinement and tunability are desirable (*104*, *107*), particularly for achieving low-threshold single-plasmon (photon) nonlinearities (*108*).

Still larger propagation lengths, in atomic van der Waals crystals (e.g., h-BN), can be achieved when light couples to pure optical phonons, giving rise to slowly propagating phonon polaritons. In this case, one of the dominant loss channels, electronic losses, is absent. This leads to propagation lengths of up to 50 μm (for incident free-space wavelengths λ_0 ~5 to 6 μm), as compared to ~2 μm (for a typical λ_0 ~10 μm) in graphene (*107*). Figure 6D illustrates how ultraslow negative-phase-velocity phonon polaritons are excited and detected in a thin h-BN waveguide exhibiting hyperbolic dispersion and deep subwavelength-scale field confinement (*109*). Owing to its layered crystal structure, h-BN is a natural material in which phonon polaritons exhibiting hyperbolic dispersion exist—and there are two types of guided slow modes: type I, when $\mathrm{Re}\{\varepsilon_z\} < 0$ and $\mathrm{Re}\{\varepsilon_x\} > 0$; and type II, when $\mathrm{Re}\{\varepsilon_z\} > 0$ and $\mathrm{Re}\{\varepsilon_x\} < 0$. Here, incident infrared light (from free space; see Fig. 6D) of frequency ω = 1563 cm^{-1} (λ ~6.4 μm) couples to and excites guided hyperbolic polariton modes in the h-BN slab, whose transverse (along z) spatial profile is shown in the right panel of Fig. 6E. Specifically, the Au film shown in this figure serves as a broadband optical antenna, converting the incident p-polarized field (E_{in}) into strongly spatially confined (high momentum) near fields at the film's rightmost edge, thereby providing the necessary momentum for coupling the free-space E_{in} field into the guided modes of the h-BN slab. Based on time-domain interferometric and scattering-type near-field microscopy measurements (Fig. 6, D and F), it was found that the group velocity of the fundamental type-I mode was as small as ~0.002c (group index ~500) and with a large lifetime of ~1.8 ps—more than an order of magnitude larger than that of SPPs in Au at visible frequencies. Furthermore, the phase velocity of this mode was found to be negative (antiparallel to the forward-longitudinal direction of the group velocity) (*109*). Both of these results were found to be in excellent agreement with theory (see, e.g., Fig. 6G). The operation of these structures is currently constrained at longer (infrared) wavelengths, and implementation in the visible regime is challenging. Furthermore, in these "phononic" materials, most of the energy is stored in the kinetic and potential energy of the oscillating ions—and not in the electric field (*32*)—which limits the maximum field enhancements that can be attained.

Conclusions and outlook

We have examined the underlying physical principles enabling broadband, ultraslow waves in subdiffraction-limited nanostructures and presented exemplary technological applications in the fields of nanophotonics, metamaterials, acoustics, and 2D materials. The structures deployed are usually geometrically smoothly varying (Fig. 1B), and the underlying wave-deceleration mechanisms inherently do not involve material-parameter (permittivity, refractive index) resonances—typically relying on antiparallel power flows in the negative- and positive-permittivity regions (Fig. 1A) or, equivalently, to negative Goos-Hänchen phase shifts at the interfaces of these media (Fig. 1C). Ultimately, material and group-velocity dispersion set a limit to the bandwidth performance that can be attained (*25*, *63*). However, it should be noted that the bandwidths attained in these structures can still, in the optical regime, be large, typically of the order of ~1 to 10 THz—orders of magnitude larger than, e.g., their atomic-media counterparts (which feature similar order-of-magnitude decelerations). Furthermore, upon suitable design, e.g., in multilayer heterostructures, the dispersion band can (for a continuous range of wave vectors) become very flat, i.e., group-velocity dispersion can be minimized (*39*)—thereby leading to enhanced bandwidth performance. This last feature—the ability to enhance and engineer bandwidth "by design" at the nanoscale—is a key characteristic of the (ultra)slow-light structures reviewed here.

Specific applications range from enhanced and more efficient nonlinear effects (*68*, *73*, *74*, *108*), to light-harvesting (*64*, *83*, *89*), biosensing (*87*, *88*), nanoimaging (*80*, *110*, *111*), optical and acoustic spectral demultiplexing (*41–43*, *55*, *56*, *61*, *62*, *64*, *68*, *75–81*, *112*), on-chip spectroscopy (*82*), nonclassical light sources (*90*, *91*), cavity-free plasmonic nanolasing (*92–94*), enhanced acoustic sensors operating beyond the noise-threshold limit (*61*, *62*), and tunable, deep-subwavelength, ultraslow guided Dirac fermions (*102*, *103*), plasmons, and surface phonon-polaritons in atomically thin crystals and heterostructures (*104–109*, *113*). Broadband slow-light effects are also attained in other structures above the diffraction limit, including photonic crystals and CROWs where broadband slow light is usually obtained with group indices of ~30 to 100 (*21–28*), and PT-symmetric structures, which can be broadband and with the light speed reducing to zero at the exceptional point (*58*, *114*). Further related schemes include broadband metamaterial and nanophotonic analogs of EIT (*115*), or suitably engineered metasurfaces to induce negative Goos-Hänchen phase shifts and achieve the same light-stopping effect but without the use of bulk negative-parameters media (*116–118*).

The broadband, ultraslow-wave regime in subdiffraction-limited nanostructures is essentially a new regime for nanophotonics, acoustics, and 2D materials, as in all three fields we have been accustomed to using fast propagating waves for diverse operations and devices. Many surprises are waiting to be revealed and further exciting applications to emerge in this new regime.

REFERENCES AND NOTES

1. A. Sommerfeld, Über die fortpflanzung des lichtes in dispergierenden medien. *Ann. Phys.* **349**, 177–202 (1914). [transl. in L. Brillouin, *Wave Propagation and Group Velocity* Ch. II (Academic Press, New York, 1960)] doi: 10.1002/andp.19143491002
2. L. Brillouin, Über die fortpflanzung des lichtes in dispergierenden medien. *Ann. Phys.* **349**, 203–240 (1914). [transl. in L. Brillouin, *Wave Propagation and Group Velocity* Ch. III (Academic Press, New York, 1960).] doi: 10.1002/andp.19143491003
3. H. A. Lorentz, Uber die Beziehung zwischen der Fortpflanzungsgeschwindigkeit des Lichtes und der Körperdichte. *Wiedemann Ann* **9**, 641–664 (1880). doi: 10.1002/andp.18802450406
4. G. M. Gehring, A. Schweinsberg, C. Barsi, N. Kostinski, R. W. Boyd, Observation of backward pulse propagation through a medium with a negative group velocity. *Science* **312**, 895–897 (2006). doi: 10.1126/science.1124524; pmid: 16690861
5. P. W. Milonni, *Fast Light, Slow Light, and Left-handed Light* (Institute of Physics, 2005).
6. J. B. Khurgin, R. S. Tucker, *Slow Light: Science and Applications* (Taylor & Francis, 2009).
7. S. Chu, S. Wong, Linear pulse propagation in an absorbing medium. *Phys. Rev. Lett.* **48**, 738–741 (1982). doi: 10.1103/PhysRevLett.48.738
8. F. R. Faxvog, C. N. Y. Chow, T. Bieber, J. A. Carruthers, Measured pulse velocity greater than c in a neon absorption cell. *Appl. Phys. Lett.* **17**, 192–193 (1970). doi: 10.1063/1.1653360
9. R. Y. Chiao, A. M. Steinberg, Tunneling times and superluminality. *Prog. Opt.* **37**, 345–405 (1997). doi: 10.1016/S0079-6638(08)70341-X
10. H. G. Winful, Nature of "superluminal" barrier tunneling. *Phys. Rev. Lett.* **90**, 023901 (2003). doi: 10.1103/PhysRevLett.90.023901; pmid: 12570546
11. L. J. Wang, A. Kuzmich, A. Dogariu, Gain-assisted superluminal light propagation. *Nature* **406**, 277–279 (2000). doi: 10.1038/35018520; pmid: 10917523
12. G. Nimtz, W. Heitmann, Superluminal photonic tunneling and quantum electronics. *Prog. Quantum Electron.* **21**, 81–108 (1997). doi: 10.1016/S0079-6727(97)84686-1
13. J. Durnin, J. Miceli Jr., J. H. Eberly, Diffraction-free beams. *Phys. Rev. Lett.* **58**, 1499–1501 (1987). doi: 10.1103/PhysRevLett.58.1499; pmid: 10034453
14. R. W. Boyd, D. J. Gauthier, Controlling the velocity of light pulses. *Science* **326**, 1074–1077 (2009). doi: 10.1126/science.1170885; pmid: 19965419
15. D. Giovannini *et al.*, Optics. Spatially structured photons that travel in free space slower than the speed of light. *Science* **347**, 857–860 (2015). doi: 10.1126/science.aaa3035; pmid: 25612608
16. I. Liberal, N. Engheta, Near-zero refractive index photonics. *Nat. Photonics* **11**, 149–158 (2017). doi: 10.1038/nphoton.2017.13
17. A. Ciattoni, A. Marini, C. Rizza, M. Scalora, F. Biancalana, Polariton excitation in epsilon-near-zero slabs: Transient trapping of slow light. *Phys. Rev. A* **87**, 053853 (2013). doi: 10.1103/PhysRevA.87.053853
18. M. H. Javani, M. I. Stockman, Real and imaginary properties of epsilon-near-zero materials. *Phys. Rev. Lett.* **117**, 107404 (2016). doi: 10.1103/PhysRevLett.117.107404; pmid: 27636495
19. L. V. Hau, S. E. Harris, Z. Dutton, C. H. Behroozi, Light speed reduction to 17 metres per second in an ultracold atomic gas. *Nature* **397**, 594–598 (1999). doi: 10.1038/17561
20. M. Klein *et al.*, Slow light in narrow paraffin-coated vapor cells. *Appl. Phys. Lett.* **95**, 091102 (2009). doi: 10.1063/1.3207825
21. T. Baba, Slow light in photonic crystals. *Nat. Photonics* **2**, 465–473 (2008). doi: 10.1038/nphoton.2008.146

22. Y. A. Vlasov, M. O'Boyle, H. F. Hamann, S. J. McNab, Active control of slow light on a chip with photonic crystal waveguides. *Nature* **438**, 65–69 (2005). doi: 10.1038/nature04210; pmid: 16267549
23. A. Yariv, Y. Xu, R. K. Lee, A. Scherer, Coupled-resonator optical waveguide: A proposal and analysis. *Opt. Lett.* **24**, 711–713 (1999). doi: 10.1364/OL.24.000711; pmid: 18073830
24. Z. Zhu, D. J. Gauthier, R. W. Boyd, Stored light in an optical fiber via stimulated Brillouin scattering. *Science* **318**, 1748–1750 (2007). doi: 10.1126/science.1149066; pmid: 18079395
25. J. T. Mok, C. M. De Sterke, I. C. M. Littler, B. J. Eggleton, Dispersionless slow light using gap solitons. *Nat. Phys.* **2**, 775–780 (2006). doi: 10.1038/nphys438
26. B. Corcoran *et al.*, Green light emission in silicon through slow-light enhanced third-harmonic generation in photonic-crystal waveguides. *Nat. Photonics* **3**, 206–210 (2009). doi: 10.1038/nphoton.2009.28
27. M. Soljačić *et al.*, Photonic-crystal slow-light enhancement of nonlinear phase sensitivity. *J. Opt. Soc. Am. B* **19**, 2052–2059 (2002). doi: 10.1364/JOSAB.19.002052
28. P. Markoš, C. M. Soukoulis, *Wave Propagation: From Electrons to Photonic Crystals and Left-Handed Materials* (Princeton Univ. Press, 2008).
29. R. Marqués, F. Martín, M. Sorolla, *Metamaterials with Negative Parameters: Theory, Design and Microwave Applications* (Wiley, 2013).
30. W. Cai, V. M. Shalaev, *Optical Metamaterials: Fundamentals and Applications* (Springer, 2010).
31. S. Bozhevolnyi, *Plasmonic Nanoguides and Circuits* (Pan Stanford, 2008).
32. J. B. Khurgin, How to deal with the loss in plasmonics and metamaterials. *Nat. Nanotechnol.* **10**, 2–6 (2015). doi: 10.1038/nnano.2014.310; pmid: 25559961
33. S. I. Bozhevolnyi, J. B. Khurgin, The case for quantum plasmonics. *Nat. Photonics* **11**, 398–400 (2017). doi: 10.1038/nphoton.2017.103
34. O. Hess *et al.*, Active nanoplasmonic metamaterials. *Nat. Mater.* **11**, 573–584 (2012). doi: 10.1038/nmat3356; pmid: 22717488
35. M. S. Tame *et al.*, Quantum Plasmonics. *Nat. Phys.* **9**, 329–340 (2013). doi: 10.1038/nphys2615
36. L. Novotny, B. Hecht, *Principles of Nano-optics* (Cambridge Univ. Press, 2012).
37. S. E. Harris, Electromagnetically induced transparency. *Phys. Today* **50**, 36–42 (1997). doi: 10.1063/1.881806
38. M. D. Lukin, A. Imamoğlu, Controlling photons using electromagnetically induced transparency. *Nature* **413**, 273–276 (2001). doi: 10.1038/35095000; pmid: 11565022
39. K. L. Tsakmakidis, T. W. Pickering, J. M. Hamm, A. F. Page, O. Hess, Completely stopped and dispersionless light in plasmonic waveguides. *Phys. Rev. Lett.* **112**, 167401 (2014). doi: 10.1103/PhysRevLett.112.167401; pmid: 24815668
40. I. V. Shadrivov, A. A. Sukhorukov, Y. S. Kivshar, Guided modes in negative-refractive-index waveguides. *Phys. Rev. E Stat. Nonlin. Soft Matter Phys.* **67**, 057602 (2003). doi: 10.1103/PhysRevE.67.057602; pmid: 12786330
41. M. I. Stockman, Nanofocusing of optical energy in tapered plasmonic waveguides. *Phys. Rev. Lett.* **93**, 137404 (2004). doi: 10.1103/PhysRevLett.93.137404; pmid: 15524758
42. K. V. Nerkararyan, Superfocusing of a surface polariton in a wedge-like structure. *Phys. Lett. A* **237**, 103–105 (1997). doi: 10.1016/S0375-9601(97)00722-6
43. K. L. Tsakmakidis, A. D. Boardman, O. Hess, 'Trapped rainbow' storage of light in metamaterials. *Nature* **450**, 397–401 (2007). doi: 10.1038/nature06285; pmid: 18004380
44. C. Helgert *et al.*, Effective properties of amorphous metamaterials. *Phys. Rev. B* **79**, 233107 (2009). doi: 10.1103/PhysRevB.79.233107
45. M. J. Adams, *An introduction to Optical Waveguides* (Wiley, 1981).
46. A. H. Cherin, *Introduction to Optical Fibers* (McGraw-Hill, 1982).
47. K. L. Tsakmakidis, A. Klaedtke, D. P. Aryal, C. Jamois, O. Hess, Single-mode operation in the slow-light regime using oscillatory waves in generalized left-handed heterostructures. *Appl. Phys. Lett.* **89**, 201103 (2006). doi: 10.1063/1.2387873
48. K. L. Tsakmakidis, C. Hermann, A. Klaedtke, C. Jamois, O. Hess, Surface plasmon polaritons in generalized slab heterostructures with negative permittivity and permeability. *Phys. Rev. B* **73**, 085104 (2006). doi: 10.1103/PhysRevB.73.085104
49. A. Reza, M. M. Dignam, S. Hughes, Can light be stopped in realistic metamaterials? *Nature* **455**, E10–E11 (2008). doi: 10.1038/nature07359
50. K. L. Tsakmakidis, A. D. Boardman, O. Hess, Can light be stopped in realistic metamaterials? *Nature* **455**, E11–E12 (2008). doi: 10.1038/nature07360
51. A. Archambault, T. V. Teperik, F. Marquier, J. J. Greffet, Surface plasmon Fourier optics. *Phys. Rev. B* **79**, 195414 (2009). doi: 10.1103/PhysRevB.79.195414
52. A. Archambault, M. Besbes, J. J. Greffet, Superlens in the time domain. *Phys. Rev. Lett.* **109**, 097405 (2012). doi: 10.1103/PhysRevLett.109.097405; pmid: 23002884
53. K. C. Huang *et al.*, Nature of lossy Bloch states in polaritonic photonic crystals. *Phys. Rev. B* **69**, 195111 (2004). doi: 10.1103/PhysRevB.69.195111
54. S. He, Y. He, Y. Jin, Revealing the truth about 'trapped rainbow' storage of light in metamaterials. *Sci. Rep.* **2**, 583 (2012). doi: 10.1038/srep00583; pmid: 22900141
55. L. Shen, X. Zheng, X. Deng, Stopping terahertz radiation without backscattering over a broad band. *Opt. Express* **23**, 11790–11798 (2015). doi: 10.1364/OE.23.011790; pmid: 25969270
56. K. Liu, S. He, Truly trapped rainbow by utilizing nonreciprocal waveguides. *Sci. Rep.* **6**, 30206 (2016). doi: 10.1038/srep30206; pmid: 27453496
57. D. Jalas *et al.*, What is – and what is not – an optical isolator. *Nat. Photonics* **7**, 579–582 (2013). doi: 10.1038/nphoton.2013.185
58. C. E. Rüter *et al.*, Observation of parity-time symmetry in optics. *Nat. Phys.* **6**, 192–195 (2010). doi: 10.1038/nphys1515
59. M. C. Rechtsman *et al.*, Photonic Floquet topological insulators. *Nature* **496**, 196–200 (2013). doi: 10.1038/nature12066; pmid: 23579677
60. A. B. Khanikaev *et al.*, Photonic topological insulators. *Nat. Mater.* **12**, 233–239 (2013). doi: 10.1038/nmat3520; pmid: 23241532
61. Y. Chen, H. Liu, M. Reilly, H. Bae, M. Yu, Enhanced acoustic sensing through wave compression and pressure amplification in anisotropic metamaterials. *Nat. Commun.* **5**, 5247 (2014). doi: 10.1038/ncomms6247; pmid: 25316410
62. J. Zhu *et al.*, Acoustic rainbow trapping. *Sci. Rep.* **3**, 1728 (2013). doi: 10.1038/srep01728
63. J. B. Khurgin, Slow light in various media: A tutorial. *Adv. Opt. Photonics* **2**, 287–318 (2010). doi: 10.1364/AOP.2.000287
64. A. Aubry *et al.*, Plasmonic light-harvesting devices over the whole visible spectrum. *Nano Lett.* **10**, 2574–2579 (2010). doi: 10.1021/nl101235d; pmid: 20518545
65. W. T. Lu, Y. J. Huang, B. D. F. Casse, R. K. Banyal, S. Sridhar, Storing light in active optical waveguides with single-negative materials. *Appl. Phys. Lett.* **96**, 211112 (2010). doi: 10.1063/1.3431574
66. W. T. Lu, S. Savo, B. D. F. Casse, S. Sridhar, Slow microwave waveguide made of negative permeability metamaterials. *Microw. Opt. Technol. Lett.* **51**, 2705–2709 (2009). doi: 10.1002/mop.24727
67. S. Savo, B. D. F. Casse, W. Lu, S. Sridhar, Observation of slow-light in a metamaterials waveguide at microwave frequencies. *Appl. Phys. Lett.* **98**, 171907 (2011). doi: 10.1063/1.3583521
68. I.-Y. Park *et al.*, Plasmonic generation of ultrashort extreme ultraviolet light pulses. *Nat. Photonics* **5**, 677–681 (2011). doi: 10.1038/nphoton.2011.258
69. K. L. Tsakmakidis *et al.*, Breaking Lorentz reciprocity to overcome the time-bandwidth limit in physics and engineering. *Science* **356**, 1260–1264 (2017). doi: 10.1126/science.aam6662; pmid: 28642432
70. C. Ciracì *et al.*, Probing the ultimate limits of plasmonic enhancement. *Science* **337**, 1072–1074 (2012). doi: 10.1126/science.1224823; pmid: 22936772
71. J. A. Scholl, A. L. Koh, J. A. Dionne, Quantum plasmon resonances of individual metallic nanoparticles. *Nature* **483**, 421–427 (2012). doi: 10.1038/nature10904; pmid: 22437611
72. K. J. Savage *et al.*, Revealing the quantum regime in tunnelling plasmonics. *Nature* **491**, 574–577 (2012). doi: 10.1038/nature11653; pmid: 23135399
73. S. Kim *et al.*, High-harmonic generation by resonant plasmon field enhancement. *Nature* **453**, 757–760 (2008). doi: 10.1038/nature07012; pmid: 18528390
74. M. Sivis, M. Duwe, B. Abel, C. Ropers, Nanostructure-enhanced atomic line emission. *Nature* **485**, E1–E2, discussion E2–E3 (2012). doi: 10.1038/nature10978; pmid: 22575967
75. Q. Gan, Z. Fu, Y. J. Ding, F. J. Bartoli, Ultrawide-bandwidth slow-light system based on THz plasmonic graded metallic grating structures. *Phys. Rev. Lett.* **100**, 256803 (2008). doi: 10.1103/PhysRevLett.100.256803; pmid: 18643690
76. Q. Gan, Y. J. Ding, F. J. Bartoli, "Rainbow" trapping and releasing at telecommunication wavelengths. *Phys. Rev. Lett.* **102**, 056801 (2009). doi: 10.1103/PhysRevLett.102.056801; pmid: 19257533
77. Z. Fu, Q. Gan, Y. J. Ding, F. J. Bartoli, From waveguiding to spatial localization of THz waves within a plasmonic metallic grating. *IEEE Sel. Topics Quantum Electron* **14**, 486–490 (2008). doi: 10.1109/JSTQE.2008.917032
78. L. Chen, G. P. Wang, Q. Gan, F. J. Bartoli, Trapping of surface-plasmon polaritons in a graded Bragg structure: Frequency-dependent spatially separated localization of the visible spectrum modes. *Phys. Rev. B* **80**, 161106 (2009). doi: 10.1103/PhysRevB.80.161106
79. V. N. Smolyaninova, I. I. Smolyaninov, A. V. Kildishev, V. M. Shalaev, Experimental observation of the trapped rainbow. *Appl. Phys. Lett.* **96**, 211121 (2010). doi: 10.1063/1.3442501
80. H. Choi, D. F. P. Pile, S. Nam, G. Bartal, X. Zhang, Compressing surface plasmons for nano-scale optical focusing. *Opt. Express* **17**, 7519–7524 (2009). doi: 10.1364/OE.17.007519; pmid: 19399129
81. X. P. Zhao *et al.*, Trapped rainbow effect in visible light left-handed heterostructures. *Appl. Phys. Lett.* **95**, 071111 (2009). doi: 10.1063/1.3211867
82. V. Smolyaninova, I. Smolyaninov, A. Kildishev, V. M. Shalaev, Trapped rainbow techniques for spectroscopy on a chip and fluorescence enhancement. *Appl. Phys. B* **106**, 577–581 (2012). doi: 10.1007/s00340-011-4856-x
83. A. I. Fernández-Domínguez, S. A. Maier, J. B. Pendry, Collection and concentration of light by touching spheres: A transformation optics approach. *Phys. Rev. Lett.* **105**, 266807 (2010). doi: 10.1103/PhysRevLett.105.266807; pmid: 21231703
84. Y. Luo, D. Y. Lei, S. A. Maier, J. B. Pendry, Broadband light harvesting nanostructures robust to edge bluntness. *Phys. Rev. Lett.* **108**, 023901 (2012). doi: 10.1103/PhysRevLett.108.023901; pmid: 22324685
85. Y. Luo, A. Aubry, J. B. Pendry, Electromagnetic contribution to surface-enhanced Raman scattering from rough metal surfaces: A transformation optics approach. *Phys. Rev. B* **83**, 155422 (2011). doi: 10.1103/PhysRevB.83.155422
86. A. C. Atre, A. García-Etxarri, H. Alaeian, J. A. Dionne, Toward high-efficiency solar upconversion with plasmonic nanostructures. *J. Opt.* **14**, 024008 (2012). doi: 10.1088/2040-8978/14/2/024008
87. Y. Lu, G. L. Liu, J. Kim, Y. X. Mejia, L. P. Lee, Nanophotonic crescent moon structures with sharp edge for ultrasensitive biomolecular detection by local electromagnetic field enhancement effect. *Nano Lett.* **5**, 119–124 (2005). doi: 10.1021/nl048232+; pmid: 15792424
88. K. Kneipp *et al.*, Extremely large enhancement factors in surface-enhanced Raman scattering for molecules on colloidal gold clusters. *Appl. Spectrosc.* **52**, 1493–1497 (1998). doi: 10.1366/0003702981943059
89. Y. Cui *et al.*, Ultrabroadband light absorption by a sawtooth anisotropic metamaterial slab. *Nano Lett.* **12**, 1443–1447 (2012). doi: 10.1021/nl204118h; pmid: 22309161
90. S.-H. Gong *et al.*, Self-aligned deterministic coupling of single quantum emitter to nanofocused plasmonic modes. *Proc. Natl. Acad. Sci. U.S.A.* **112**, 5280–5285 (2015). doi: 10.1073/pnas.1418049112; pmid: 25870303
91. O. Hess, K. L. Tsakmakidis, Metamaterials with quantum gain. *Science* **339**, 654–655 (2013). doi: 10.1126/science.1231254; pmid: 23393252
92. K. L. Tsakmakidis *et al.*, Plasmonic nanolasers without cavity, threshold and diffraction limit using stopped light, in *Frontiers in Optics 2012* (Rochester, New York, USA, 2012), paper FTh2A.2.
93. T. Pickering, J. M. Hamm, A. F. Page, S. Wuestner, O. Hess, Cavity-free plasmonic nanolasing enabled by dispersionless stopped light. *Nat. Commun.* **5**, 4972 (2014). doi: 10.1038/ncomms5972; pmid: 25230337
94. S. Wuestner *et al.*, Ultrafast dynamics of nanoplasmonic stopped-light lasing. *Faraday Discuss.* **178**, 307–324 (2015). doi: 10.1039/C4FD00181H; pmid: 25778453

95. H. Choo *et al*., Nanofocusing in a metal-insulator-metal gap plasmon waveguide with a three-dimensional linear taper. *Nat. Photonics* **6**, 838–844 (2012). doi: 10.1038/nphoton.2012.277
96. A. Melikyan *et al*., High-speed plasmonic phase modulators. *Nat. Photonics* **8**, 229–233 (2014). doi: 10.1038/nphoton.2014.9
97. Q. Gan *et al*., Experimental verification of the rainbow trapping effect in adiabatic plasmonic gratings. *Proc. Natl. Acad. Sci. U.S.A.* **108**, 5169–5173 (2011). doi: 10.1073/pnas.1014963108; pmid: 21402936
98. Z. H. Fang, H. Chen, F. S. Yang, C. R. Luo, X. P. Zhao, Slowing down light using a dendritic cell cluster metasurface waveguide. *Sci. Rep.* **6**, 37856 (2016). doi: 10.1038/srep37856; pmid: 27886279
99. E. Laux, C. Genet, T. Skauli, T. W. Ebbesen, Plasmonic photon sorters for spectral and polarimetric imaging. *Nat. Photonics* **2**, 161–164 (2008). doi: 10.1038/nphoton.2008.1
100. M. H. Kryder *et al*., Heat assisted magnetic recording. *Proc. IEEE* **96**, 1810–1835 (2008). doi: 10.1109/JPROC.2008.2004315
101. W. A. Challener *et al*., Heat-assisted magnetic recording by a near-field transducer with efficient optical energy transfer. *Nat. Photonics* **3**, 220–224 (2009). doi: 10.1038/nphoton.2009.26
102. C. W. J. Beenakker, R. A. Sepkhanov, A. R. Akhmerov, J. Tworzydło, Quantum Goos-Hänchen effect in graphene. *Phys. Rev. Lett.* **102**, 146804 (2009). doi: 10.1103/PhysRevLett.102.146804; pmid: 19392468
103. L. Zhao, S. F. Yelin, Proposal for graphene-based coherent buffers and memories. *Phys. Rev. B* **81**, 115441 (2010). doi: 10.1103/PhysRevB.81.115441
104. A. Woessner *et al*., Highly confined low-loss plasmons in graphene-boron nitride heterostructures. *Nat. Mater.* **14**, 421–425 (2015). doi: 10.1038/nmat4169; pmid: 25532073
105. A. K. Geim, I. V. Grigorieva, Van der Waals heterostructures. *Nature* **499**, 419–425 (2013). doi: 10.1038/nature12385; pmid: 23887427
106. A. Poddubny, I. Iorsh, P. Belov, Y. Kivshar, Hyperbolic metamaterials. *Nat. Photonics* **7**, 948–957 (2013). doi: 10.1038/nphoton.2013.243
107. S. Dai *et al*., Graphene on hexagonal boron nitride as a tunable hyperbolic metamaterial. *Nat. Nanotechnol.* **10**, 682–686 (2015). doi: 10.1038/nnano.2015.131; pmid: 26098228
108. M. Gullans, D. E. Chang, F. H. L. Koppens, F. J. García de Abajo, M. D. Lukin, Single-photon nonlinear optics with graphene plasmons. *Phys. Rev. Lett.* **111**, 247401 (2013). doi: 10.1103/PhysRevLett.111.247401; pmid: 24483697
109. E. Yoxall *et al*., Direct observation of ultraslow hyperbolic polariton propagation with negative phase velocity. *Nat. Photonics* **9**, 674–678 (2015). doi: 10.1038/nphoton.2015.166
110. A. Giugni *et al*., Hot-electron nanoscopy using adiabatic compression of surface plasmons. *Nat. Nanotechnol.* **8**, 845–852 (2013). doi: 10.1038/nnano.2013.207; pmid: 24141538
111. M. Sandtke, L. Kuipers, Slow guided surface plasmons at telecom frequencies. *Nat. Photonics* **1**, 573–576 (2007). doi: 10.1038/nphoton.2007.174
112. A. C. Atre *et al*., Nanoscale optical tomography with cathodoluminescence spectroscopy. *Nat. Nanotechnol.* **10**, 429–436 (2015). doi: 10.1038/nnano.2015.39; pmid: 25849788
113. S. Dai *et al*., Tunable phonon polaritons in atomically thin van der Waals crystals of boron nitride. *Science* **343**, 1125–1129 (2014). doi: 10.1126/science.1246833; pmid: 24604197
114. R. El-Ganainy, K. G. Makris, D. N. Christodoulides, Z. H. Musslimani, Theory of coupled optical PT-symmetric structures. *Opt. Lett.* **32**, 2632–2634 (2007). doi: 10.1364/OL.32.002632; pmid: 17767329
115. C. Wu, A. B. Khanikaev, G. Shvets, Broadband slow light metamaterial based on a double-continuum Fano resonance. *Phys. Rev. Lett.* **106**, 107403 (2011). doi: 10.1103/PhysRevLett.106.107403; pmid: 21469834
116. R. Yang, W. Zhu, J. Li, Realization of "trapped rainbow" in 1D slab waveguide with surface dispersion engineering. *Opt. Express* **23**, 6326–6335 (2015). doi: 10.1364/OE.23.006326; pmid: 25836853
117. N. Yu, F. Capasso, Flat optics with designer metasurfaces. *Nat. Mater.* **13**, 139–150 (2014). doi: 10.1038/nmat3839; pmid: 24452357
118. A. V. Kildishev, A. Boltasseva, V. M. Shalaev, Planar photonics with metasurfaces. *Science* **339**, 1232009 (2013). doi: 10.1126/science.1232009; pmid: 23493714

ACKNOWLEDGMENTS

We acknowledge useful discussions with J. Pendry on transformation-optics slow-light structures, and with E. Yablonovitch on the slow-light physics of the Seagate Technology HAMR devices. This work was primarily funded by the Director, Office of Science, Office of Basic Energy Sciences, Materials Sciences and Engineering Division, of the U.S. Department of Energy under contract no. DE-AC02-05-CH11231. It was further supported by the Office of Naval Research (ONR) MURI program under grant no. N00014-13-1-0678, the Leverhulme Trust, the UK Engineering and Physical Sciences Research Council (EPSRC) under grants EP/L024926/1 and EP/L027151/1, the Canada Excellence Research Chairs Program, and the Eugen Lommel fellowship of the Max Planck Institute for the Science of Light, Erlangen, Germany.

10.1126/science.aan5196

Science

Ultraslow waves on the nanoscale

Kosmas L. Tsakmakidis, Ortwin Hess, Robert W. Boyd and Xiang Zhang

Science **358** (6361), eaan5196.
DOI: 10.1126/science.aan5196

Slow light on the nanoscale

When light passes through an optical material, its speed is reduced by the refractive index of that material. Under exceptional circumstances, light can be slowed to a walking pace or even stopped momentarily. Exploring approaches for practical applications, Tsakmakidis *et al.* review how the speed of light can be controlled using designed materials and fabricated structures. They show how the combination of slow light and nanotechnology gives rise to a number of effects of interest in signal processing and optoelectronic communication.

Science, this issue p. eaan5196